The Astrophysical Journal, 762:25 (16pp), 2013 January 1 doi:10.1088/0004-637X/762/1/25

THE MOST METAL-POOR STARS. I. DISCOVERY, DATA, AND ATMOSPHERIC PARAMETERS*

John E. Norris[1], M. S. Bessell[1], David Yong[1], N. Christlieb[2], P. S. Barklem[3], M. Asplund[1,4], Simon J. Murphy[1], Timothy C. Beers[5,6], Anna Frebel[7], and S. G. Ryan[8]
[1] Research School of Astronomy and Astrophysics, The Australian National University, Weston, ACT 2611, Australia; jen@mso.anu.edu.au, bessell@mso.anu.edu.au, yong@mso.anu.edu.au, martin@mso.anu.edu.au
[2] Zentrum für Astronomie der Universität Heidelberg, Landessternwarte, Königstuhl 12, D-69117 Heidelberg, Germany; n.christlieb@lsw.uni-heidelberg.de
[3] Department of Physics and Astronomy, Uppsala University, Box 515, SE-75120 Uppsala, Sweden; paul.barklem@physics.uu.se
[4] Max Planck Institute for Astrophysics, Postfach 1317, D-85741 Garching, Germany
[5] National Optical Astronomy Observatory, Tucson, AZ 85719, USA
[6] Department of Physics and Astronomy and JINA: Joint Institute for Nuclear Astrophysics, Michigan State University, East Lansing, MI 48824, USA; beers@pa.msu.edu
[7] Department of Physics, Massachusetts Institute of Technology, Cambridge, MA 02139, USA; afrebel@mit.edu
[8] Centre for Astrophysics Research, School of Physics, Astronomy and Mathematics, University of Hertfordshire, College Lane, Hatfield, Hertfordshire, AL10 9AB, UK; s.g.ryan@herts.ac.uk
Received 2012 April 12; accepted 2012 August 6; published 2012 December 13

ABSTRACT

We report the discovery of 34 stars in the Hamburg/ESO Survey for metal-poor stars and the Sloan Digital Sky Survey that have [Fe/H] $\lesssim -3.0$. Their median and minimum abundances are [Fe/H] $= -3.1$ and -4.1, respectively, while 10 stars have [Fe/H] < -3.5. High-resolution, high signal-to-noise spectroscopic data—equivalent widths and radial velocities—are presented for these stars, together with an additional four objects previously reported or currently being investigated elsewhere. We have determined the atmospheric parameters, effective temperature ($T_{\rm eff}$), and surface gravity ($\log g$), which are critical in the determination of the chemical abundances and the evolutionary status of these stars. Three techniques were used to derive these parameters. Spectrophotometric fits to model atmosphere fluxes were used to derive $T_{\rm eff}$, $\log g$, and an estimate of $E(B-V)$; Hα, Hβ, and Hγ profile fitting to model atmosphere results provided the second determination of $T_{\rm eff}$ and $\log g$; and finally, we used an empirical $T_{\rm eff}$-calibrated Hδ index, for the third, independent $T_{\rm eff}$ determination. The three values of $T_{\rm eff}$ are in good agreement, although the profile fitting may yield systematically cooler $T_{\rm eff}$ values, by $\sim$100 K. This collective data set will be analyzed in future papers in the present series to utilize the most metal-poor stars as probes of conditions in the early universe.

Key words: early universe – Galaxy: formation – Galaxy: halo – stars: abundances – stars: fundamental parameters

Online-only material: color figures, machine-readable tables

1. INTRODUCTION

Six decades after the discovery of metal-poor stars by Chamberlain & Aller (1951), the study of these objects has become a mature area of research. In 2010, high-resolution, high signal-to-noise (S/N) chemical abundance analyses existed for some 400 stars that have [Fe/H] < -2.5, some 24 with [Fe/H] < -3.5, and 3 having [Fe/H] < -4.5 (see the compilation of Frebel (2010, https://www.cfa.harvard.edu/~afrebel/). As discussed by many authors, the most metal-poor stars, believed to have formed at redshifts $z \gtrsim 6$, are among the best probes of conditions in the early universe, including in particular the formation of the first stars and the first chemical elements. We shall not repeat here the case for this endeavor, but refer the reader to earlier works (see, e.g., Bessell & Norris 1984; McWilliam et al. 1995; Ryan et al. 1996; Norris et al. 2001; Cayrel et al. 2004; Beers & Christlieb 2005; Cohen et al. 2008; Lai et al. 2008; Frebel & Norris 2011) for a thorough discussion of the rationale that drives this very active field.

The aim of the present series of papers is to increase the inventory of the most metal-poor stars, by which we mean [Fe/H] $\lesssim -3.5$, in order to understand the metallicity distribution function (MDF) at lowest metallicity and to investigate abundance patterns that contain clues to conditions at the earliest times. We are interested to gain insight into the relative abundances ([X/Fe][9]) in this abundance regime, involving in particular C, N, O, Mg, Na, Al, and the heavy neutron-capture elements, which deviate strongly from the relatively well-defined behavior of the majority of stars in the ([X/Fe], [Fe/H])—planes at higher abundances ([Fe/H] > -3.5) (see, e.g., Norris et al. 2007, Figure 11).

Section 2 of the paper is concerned with the discovery of stars having [Fe/H] < -3.0, by obtaining medium-resolution spectra of candidate metal-poor stars. Section 3 describes follow-up high-resolution, high-S/N spectroscopy of the most metal-poor of them, together with the reduction and analysis of the spectra to produce the basic data (equivalent widths and radial velocities) upon which subsequent analyses will be based. Our sample contains 38 stars, some 13 of which (12 identified in the endeavors described in Section 2) have [Fe/H] < -3.5, based on subsequent high-resolution, high-S/N spectroscopic analysis. In Section 4, we describe the determination of accurate effective temperatures needed for the chemical abundance analysis. Papers II, III (Yong et al. 2013a, 2013b) and Papers IV, V (Norris et al. 2013; J. E Norris et al., in preparation) will present

* This paper includes data obtained with the ANU 2.3 m Telescope at Siding Spring Observatory, Australia; the Magellan Clay Telescope at Las Campanas Observatory, Chile; the Keck I Telescope at the W. M. Keck Observatory, Hawaii, USA; and the VLT (Kueyen) of the European Southern Observatory, Paranal, Chile (proposal 281.D-5015).

[9] $[{\rm X/Fe}] = \log_{10}(N_{\rm X}/N_{\rm Fe})_{\star} - \log_{10}(N_{\rm X}/N_{\rm Fe})_{\odot}$.

accurate chemical abundances and discussion of the elements from lithium through to the heavy-neutron-capture elements.

2. DISCOVERY AND SELECTION OF PROGRAM STARS

The present program represents the completion of a search over some 30 years for the most metal-poor stars undertaken at the Mount Stromlo & Siding Spring Observatories, ANU (now known as RSAA, ANU), based on techniques involving (in the main part) high-proper-motion stars (the NLTT survey; Luyten 1979, 1980) and metal-weak candidates obtained from Schmidt wide-field objective-prism surveys (the HK Survey (Beers et al. 1985; Beers et al. 1992)) and the Hamburg/ESO Survey (HES (Christlieb et al. 2008)).

Results based at least in part on these efforts have already been presented by Aoki et al. (2002, 2006), Bessell & Norris (1984), Cayrel et al. (2004), Christlieb et al. (2002, 2004), Frebel et al. (2005, 2006, 2007a, 2007b), Honda et al. (2004), Li et al. (2010), Norris et al. (1985, 1999, 2001, 2007), Ryan & Norris (1991), Ryan et al. (1991, 1996), and Schörck et al. (2009). These include the discovery and analysis of three of the four most metal-poor stars currently known:[10] HE 0107−5240 with [Fe/H] = –5.3 (Christlieb et al. 2002, 2004), HE 1327−2326 with [Fe/H] = –5.4 (Frebel et al. 2005; Aoki et al. 2006), and HE 0557−4840 with [Fe/H] = −4.8 (Norris et al. 2007).

The current sample of the most metal-poor stars is based principally on a medium-resolution spectroscopic survey of metal-poor candidates from the HES, supplemented by a few stars known to be extremely metal-poor from other sources.

2.1. Medium-resolution Spectroscopy with the ANU 2.3 m Telescope

Metal-poor candidates from the Hamburg/ESO objective-prism survey have been observed during the present investigation with the Australian National University's 2.3 m Telescope/Double Beam Spectrograph combination on Siding Spring Mountain, during observing sessions in 2005–2009. The spectra have a resolving power $R \sim 1600$, and cover the wavelength range 3600–5400 Å. They were reduced with the FIGARO package (http://www.aao.gov.au/figaro) and flat fielded and wavelength calibrated by using spectra of quartz and Fe–Ar lamps, respectively. Following Beers et al. (1999, their Table 2), we measured the Ca II K line index, K′, the CH *G*-band index, G′, and the hydrogen indices Hγ and Hδ to form H′, the mean of the two estimates. (H′ was not measured for objects with G′ > 4.0 Å, for which the index is affected by strong CH absorption). We used these data, following the precepts of Beers et al., to obtain estimates of iron abundance, here designated $[Fe/H]_K$. Analysis of some of these spectra have also been used for discussion of the MDF of the Galactic halo by Schörck et al. (2009) and Li et al. (2010), to which we refer the reader. For the present work, we recall that we were interested in discovering stars with [Fe/H] $\lesssim$ –3.0, and have adopted techniques that differ in two respects from those works. First, our investigation used the original abundance calibration of Beers et al. (1999). Second, that technique requires values not only of K′ but also of $(B-V)_0$. For $(B-V)_0 \lesssim 0.70$ we used the hydrogen index, when available, to provide the color estimate:[11] $(B-V)_0 = 0.840 - 0.1541H' + 0.01148H'^2$; otherwise, we used $(B-V)_{HES}$ from the HES survey (see Christlieb et al. 2008), corrected for reddening following Schlegel et al. (1998).

In what follows we present data for stars that were discovered to have $[Fe/H]_K \lesssim -3.0$, based on the above medium-resolution spectroscopy obtained in 2005–2008. Results for some extremely metal-poor stars that were observed in 2005 (e.g., HE 0557−4840, [Fe/H] = −4.8) have already been published (Norris et al. 2007) or are the subject of analysis currently underway (García Pérez et al. 2008). Follow-up investigation of objects observed in 2009 is work for the future.

During 2005–2009 we obtained some 3400 spectra of HES metal-poor candidates with the 2.3 m Telescope, and from those observed in 2005–2008 selected the 1460 stars that satisfy the following criteria: (1) *B* magnitudes in the range $12.6 < B_{HES} < 16.5$; (2) H′, the mean of the Beers et al. (1999) hydrogen Hγ and Hδ indices, less than 5.5 Å (i.e., $(B-V)_0 \gtrsim 0.34$) and $(B-V)_{HES} \gtrsim 0.30$; (3) photon counts at 4100 Å greater than 200 per ∼1 Å pixel; and (4) spectra exhibit no anomalies such as hydrogen or Ca II emission. The first criterion was chosen to discover metal-poor stars that could be observed with 6–10 m class telescopes to obtain spectra at high resolution and high-S/N in times less than a few hours; the second confines the selection almost exclusively to main-sequence dwarfs, and to red giant branch and red horizontal branch stars; and the third accepts medium-resolution spectra with sufficient S/N to produce abundance accuracy of Δ[Fe/H] ∼ 0.2–0.3 dex—at least for stars that are not carbon-rich (and for which abundances from medium-resolution spectroscopy are less well determined). For the 24 HES dwarfs and giants in the present sample with the CH *G*-band index G′< 1.5 Å, the dispersion of the differences between the present values of $[Fe/H]_K$ and those we obtain from the analysis of our high-resolution, high-S/N spectra is 0.30 dex, while for the remaining seven (carbon-rich) objects, which have G′ > 3.5 Å, the dispersion of the abundance differences is 0.40 dex.

In Figure 1, we present stars having $[Fe/H]_K < -2.5$ in the G′ (carbon-sensitive index) versus $[Fe/H]_K$ plane, where the top panel contains objects with $(B-V)_0 > 0.55$ (principally giants) and the middle panel shows those with $(B-V)_0 < 0.55$ (principally dwarfs). The sloping lines in the two panels are arbitrarily chosen to separate potentially carbon-normal and carbon-rich objects, while the vertical lines are included to emphasize the region of immediate interest for the present investigation—$[Fe/H]_K < -3.0$. More metal-poor than this limit, our 2.3 m sample survey contains 109 stars. In Figure 1 we identify those objects with $[Fe/H]_K \lesssim -3.0$ for which high-resolution, high-S/N data have been obtained in the present work, together with those of Norris et al. (2007) and García Pérez et al. (2008), as filled star symbols. Open circles represent stars for which high-resolution data are not yet available.

The bottom panel in Figure 1 presents the MDF of all of the stars in the upper two panels, where the upper thick line represents the distribution for the complete sample of stars from the 2.3 m HES sample described above, and the lower thick line shows that of only the stars having high-resolution data. The thin, mostly horizontal line in the figure shows the completeness function from Schörck et al. (2009) and Li et al. (2010) for the detection of metal-poor stars in medium-resolution investigations of the HES: below [Fe/H] = –3.0, the HES is essentially complete. Consideration of the thick lines in the figure shows quite clearly the strong bias we have introduced into the completeness function by our emphasis on observing the

[10] For details of the fourth star, SDSS J102915+172927, see Caffau et al. (2011).

[11] Based on colors and reddenings of high-proper-motion stars presented by Carney et al. (1994), together with values of K′ we obtained with the equipment described above as part of another investigation.

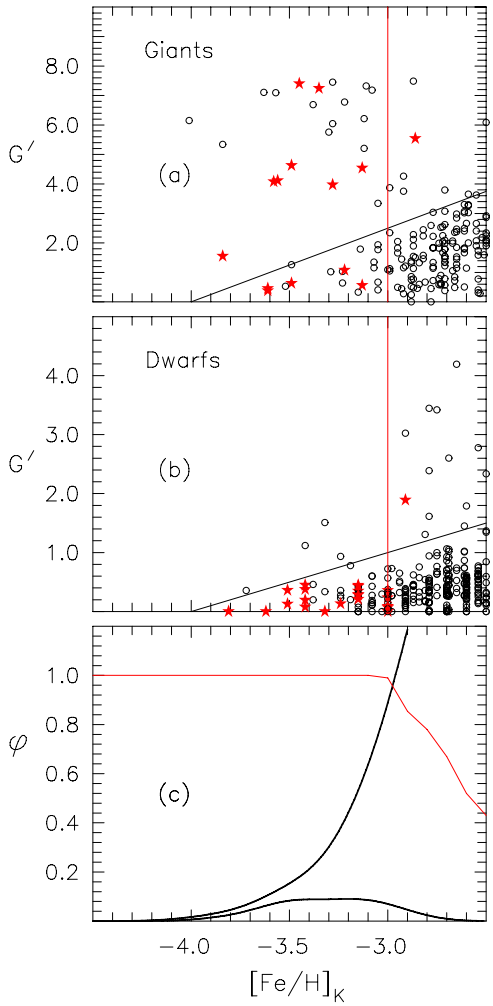

Figure 1. G′ vs. $[Fe/H]_K$ for (a) giants and (b) dwarfs in the Hamburg/ESO survey, measured on medium-resolution spectra obtained with the ANU 2.3 m Telescope. Filled (red) symbols represent stars for which high-resolution, high-S/N spectra have been obtained (in both this and other investigations). Panel (c) presents the generalized histograms (Gaussian kernel with $\sigma = 0.15$) of the MDF for stars in the medium-resolution (upper thick line) and high-resolution (lower thick line) samples. The scale of the ordinate is arbitrary, but is normalized so that the areas under the two distributions have the same proportionality to the numbers of stars in the samples. The principally horizontal, thin line represents the completeness function of the MDF obtained from medium-resolution spectroscopy of the HES, as discussed in the text. (The ordinate runs between 0. and 1.15).

(A color version of this figure is available in the online journal.)

most metal-poor stars. We shall bear this in mind in subsequent discussions of the MDF at the lowest metallicities.

2.2. Supplementary Selection

We augmented our program sample by the inclusion of eight stars from other sources. These comprise four stars from the Sloan Digital Sky Survey (SDSS; York et al. 2000), three dwarfs (BS 16545−089 and HE 1346−0427 from Cohen et al. (2004), and HE 0945−1435 from García Pérez et al. (2008)), and the red giant CS 30336−049 (Tanner et al. 2006; Lai et al. 2008).

2.3. The Sample

Our total sample thus comprises 38 stars—30 from the 2.3 m survey described in Section 2.1, 4 from the SDSS, BS 16545−089 and CS 30336−049 for the HK survey, and HE 0945−1435 and HE 1346−0427 from the HES. The basic data for these stars are presented in Table 1. Columns 1–3 contain the star names and coordinates; Columns 4–6 contain B_{HES}, $(B - V)_0$, and the source of the color; and Columns 7–10 present K′, G′, H′, and $[Fe/H]_K$, respectively. (We note that the first four entries in the table are based on spectra taken from the SDSS archives.) For completeness and comparison purposes, Column 11 presents values of [Fe/H] from Paper II, which result from the model atmosphere analysis of the high-resolution, high-S/N spectra presented here. Of these stars, 34 are original to the present work.

3. HIGH-RESOLUTION SPECTROSCOPY

3.1. Magellan, Keck, and VLT Spectra

High-resolution, high-S/N spectra of the 38 program stars in Table 1 were obtained with the Magellan/MIKE, the Keck/HIRES, and VLT/UVES telescope/spectrograph combinations during 2007–2008. Details of the observing sessions and instrumental setups are presented in Table 2, where Columns 1–4 present the telescope/spectrograph combinations, observing dates, wavelength ranges, and resolving powers ($R = \lambda/(\Delta\lambda)$), respectively.

The Magellan and Keck observations were obtained in Visitor Mode, during which data were also obtained of "standard" metal-poor stars for comparison purposes, together with quartz-iodine and ThAr lamps for flat-fielding and wavelength calibration. We tailored data acquisition for the program stars to obtain S/N $\sim$ 100 pixel^{-1} at 4500 Å for the most metal-poor stars in our sample. To do this we began our observations of each star in "snapshot" mode with a minimal number ($\sim$1–3) of 1800 s exposures, which we reduced in real time to permit us, by comparison with our library of high-resolution extremely metal-poor stars, to give priority to the more metal-poor objects.

We then obtained additional exposures as necessary to yield higher S/N for the most interesting objects. The reader will see this reflected to some extent in the S/N values reported below. The data were processed with standard IRAF[12] procedures (supplemented by the cosmic-ray removal algorithm of Pych 2004) to obtain flat-fielded, wavelength-calibrated, comic-ray-corrected, co-added, and continuum-normalized spectra (see, e.g., Yong et al. 2003).

Four exposures were obtained for HE 1506−0113 in Service Mode with the VLT/UVES system, each having an integration time of 2500 s, with spectrograph settings as used in our investigation of HE 0557−4840 (Norris et al. 2007). These four ESO pipeline-reduced spectra were co-added to produce the final spectrum, which was then continuum normalized.

Examples of the high-resolution spectra are presented in the lower panels of Figure 2, which cover the wavelength range 3900–4000 Å, together in the upper panels with the corresponding medium-resolution spectra (3800–4600 Å) described in Section 2.1. The S/N (per 0.017 Å pixel at 4500 Å) of the final high-resolution spectra are presented in the first row of each of Tables 3–6. The range in S/N for the total sample is 23–210, with median 61, while for stars with high-resolution abundances [Fe/H] < -3.5 the median S/N is 118. For the latter group, we note for the record that the mean B magnitude is 15.3.

[12] IRAF is distributed by the National Optical Astronomy Observatory, which is operated by the Association of Universities for Research in Astronomy, Inc., under cooperative agreement with the National Science Foundation.

Table 1
The Sample of 38 Extremely Metal-poor Stars

Star	R.A. (2000)	Decl. (2000)	B_{HES}	$(B-V)_0$	S[a]	K′ (Å)	G′ (Å)	H′ (Å)	$[Fe/H]_K$	[Fe/H]
(1)	(2)	(3)	(4)	(5)	(6)	(7)	(8)	(9)	(10)	(11)
52972−1213−507[b]	09 18 49.9	+37 44 27	16.2[c]	0.42	1	0.81	3.88	3.77	−3.32	−2.98
53327−2044−515[b]	01 40 36.2	+23 44 58	15.6[c]	0.51	1	0.90	0.50	2.69	−3.49	−4.04[d]
53436−1996−093[b]	11 28 13.5	+38 41 49	15.8[c]	0.38	1	0.45	0.10	4.48	−3.81	−3.53
54142−2667−094[b]	08 51 36.7	+10 18 03	15.4[c]	0.38	1	0.92	0.00	4.39	−3.24	−2.96
BS 16545−089	11 24 27.6	+36 50 28	14.8[c]	0.38	2	...	...	...	...	−3.44
CS 30336−049	20 45 23.5	−28 42 36	14.9[c]	0.86	3	1.68	0.21	0.80	−3.82	−4.10
HE 0049−3948	00 52 13.4	−39 32 37	15.6	0.35	1	0.50	0.08	5.11	−3.42	−3.68
HE 0057−5959	00 59 54.1	−59 43 30	16.4	0.61	1	0.85	0.38	1.68	−3.61	−4.08
HE 0102−1213	01 05 28.0	−11 57 29	14.1	0.43	1	1.03	0.29	3.66	−3.15	−3.28
HE 0146−1548	01 48 34.7	−15 33 25	16.5	0.89	4	3.09	4.08	0.78	−3.58	−3.46
HE 0207−1423	02 10 00.7	−14 09 12	15.8	0.82	4	2.63	7.40	2.29	−3.45	−2.95
HE 0228−4047	02 30 33.6	−40 33 56	15.5	0.34	1	0.41	0.00	5.34	−3.62	−3.75[d]
HE 0231−6025	02 32 30.7	−60 12 11	15.1	0.35	1	0.71	0.45	5.03	−3.42	−3.10
HE 0253−1331	02 56 06.6	−13 19 27	15.9	0.36	1	0.89	0.43	4.96	−3.15	−3.01
HE 0314−1739	03 17 01.8	−17 28 56	16.5	0.36	1	0.64	0.38	5.00	−3.42	−2.86
HE 0355−3728	03 57 23.0	−37 20 23	16.3	0.41	1	0.90	0.00	3.94	−3.32	−3.41[d]
HE 0945−1435	09 47 50.7	−14 49 07	15.1	0.39	1	0.69	0.13	4.27	−3.51	−3.78[d]
HE 1055+0104	10 58 04.4	+00 48 36	14.6	0.40	1	1.23	0.36	4.21	−3.00	−2.88[d]
HE 1116−0054	11 18 47.8	−01 11 20	16.5	0.39	1	0.45	0.00	4.28	−3.81	−3.48[d]
HE 1142−1422	11 44 59.3	−14 38 49	14.7	0.40	1	1.17	0.00	4.12	−3.00	−2.84
HE 1201−1512	12 03 37.1	−15 29 32	14.2	0.50	1	0.93	0.63	2.73	−3.49	−3.89[d]
HE 1204−0744	12 06 46.2	−08 00 43	15.2	0.37	1	0.92	0.34	4.60	−3.15	−2.71
HE 1207−3108	12 09 54.1	−31 25 11	12.9	0.63	1	1.69	0.56	1.53	−3.13	−2.70
HE 1320−2952	13 22 55.0	−30 08 06	14.5	0.68	1	1.82	1.08	1.14	−3.22	−3.69
HE 1346−0427	13 49 25.2	−04 42 15	14.5	0.45	4	...	...	...	...	−3.58[d]
HE 1402−0523	14 04 37.9	−05 38 13	15.8	0.38	1	0.86	0.13	4.50	−3.24	−3.18[d]
HE 1506−0113	15 09 14.3	−01 24 57	15.4	0.64	1	1.48	3.97	1.42	−3.28	−3.54
HE 2020−5228	20 24 17.0	−52 19 03	16.3	0.38	1	1.00	0.07	4.48	−3.00	−2.93
HE 2032−5633	20 36 24.9	−56 23 05	15.2	0.36	1	0.75	0.21	4.97	−3.15	−3.63
HE 2047−5612	20 51 22.2	−56 00 52	15.5	0.44	1	1.09	0.28	3.54	−3.15	−3.14
HE 2135−1924	21 38 04.7	−19 11 04	15.7	0.37	1	0.60	0.19	4.69	−3.42	−3.31
HE 2136−6030	21 40 39.7	−60 16 27	15.9	0.38	1	1.21	0.23	4.54	−3.00	−2.88
HE 2139−5432	21 42 42.5	−54 18 43	15.9	0.51	4	0.83	4.63	3.49	−3.49	−4.02
HE 2141−0726	21 44 06.6	−07 12 49	15.7	0.38	1	1.21	0.09	4.54	−3.00	−2.72
HE 2142−5656	21 46 20.5	−56 42 18	14.4	0.71	4	4.06	5.54	1.08	−2.86	−2.87
HE 2202−4831	22 06 06.0	−48 16 53	16.3	0.71	4	1.88	7.24	2.33	−3.35	−2.78
HE 2246−2410	22 48 59.7	−23 54 38	15.7	0.35	1	0.92	0.44	5.12	−3.15	−2.96
HE 2247−7400	22 51 19.6	−73 44 24	14.4	1.02	4	4.49	4.54	1.00	−3.13	−2.87

Notes.
[a] Source of $(B-V)_0$: 1 = H′, see Section 2.1; 2 = Cohen et al. (2004); 3 = Norris et al. (1999); 4 = $(B-V)_{HES}$, see Section 2.1.
[b] SDSS "MJD-plug plate-fiber" nomenclature.
[c] B from SDSS (rows (1)–(4)); Cohen et al. (2008) (row (5), adopting color from this table); and Norris et al. (1999) (row (6)).
[d] Average of dwarf and subgiant values of [Fe/H] from Table 1 of Paper II.

3.2. Equivalent Widths

Equivalent widths have been measured from these spectra as described in Norris et al. (2010a, 2010b), to whom we refer the reader for details. As noted there, we begin with the line list of Cayrel et al. (2004), which we supplement here with lines of Sr II and Ba II.[13] We also recall that the spectra of carbon-rich stars can be heavily contaminated by CH lines. To minimize this effect we followed the spectrum synthesis technique of Norris et al. (2010b) to determine when the blending of CH lines with atomic features would contaminate the latter. For stars having $G' > 3.5$ Å, we did not measure atomic features susceptible to such contamination. We also excluded lines in regions with observed C_2 absorption in these objects.

For 37 of the program objects, each spectrum was measured independently by J.E.N. and D.Y., using techniques described by Norris et al. (2001) and Yong et al. (2008).[14] In general, the agreement between the results was excellent, an example of which is shown for a representative program star in Figure 3(a). For the 37 objects, the median rms scatter between the two authors was 2.7 mÅ. We also estimated the smallest equivalent width that we could reliably measure in each of the spectra, which we present in the second row of each of Tables 3–6. (The median smallest equivalent width for our sample is 10 mÅ, while for stars having [Fe/H] < −3.5 it is 6 mÅ—driven by our emphasis on obtaining higher S/N for the more metal-poor stars in our sample.) Our adopted equivalent widths are the simple average of the results of J.E.N. and

[13] We note for completeness that we also sought, unsuccessfully, to measure lines of La II, Ce II, Nd II, and Eu II.

[14] The line strengths of HE 1506−0113 were measured by only J.E.N.

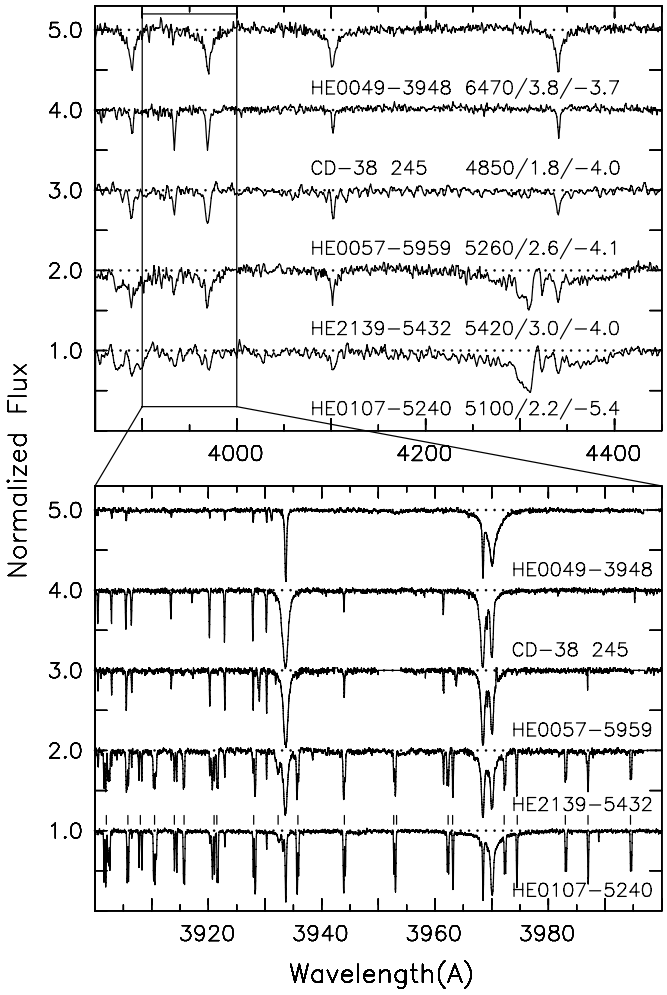

Figure 2. Spectra of some of the most metal-poor stars. HE 0049−3948, HE 0057−5959, and HE 2139−5432 are from the present work, while CD−38° 245 and HE 0107−5240 derive from Bessell & Norris (1984) and Christlieb et al. (2004), respectively, and are shown for comparison purposes. The upper panel presents medium-resolution ($R \sim 1600$) spectra obtained with the 2.3 m Telescope and covers the range 3850–4450 Å. The numbers in the panel represent $T_{\rm eff}$/log g/[Fe/H] from analyses of high-resolution, high-S/N, spectra by Christlieb et al. (2004), Norris et al. (2001), the present work, and Paper II. The lower panel shows spectra of the same stars at $R \sim 40{,}000$ on the range 3900–4000 Å. The reader will note that while the Ca II H & K lines (at 3968.4 and 3933.6 Å, respectively) are very weak in the most metal-poor giant, HE 0107−5240, many more lines have appeared in its spectrum. These are features of CH (the positions of which are indicated immediately above the spectrum) resulting from an extremely large overabundance of carbon relative to iron in this object. We note that HE 2139−5432 is similar to HE 0107−5240 in this respect, but not as metal-poor.

D.Y. for each star. These are presented in Tables 3–6, which contain line strengths for 14 elements in the wavelength range ∼3750–6500 Å. Columns 1–4 contain line identification, lower excitation potential (χ), and log gf value, respectively, for 191 unblended lines suitable for model atmosphere abundance analysis, taken from Cayrel et al. (2004, Table 3), together with values from the literature for Sr II and Ba II.[15] The remainder of the table is populated by equivalent widths. Some of the lines lead to significantly discrepant abundances compared with those obtained from other lines of the same species. We flag these values in Tables 3–6, and have excluded them from the analysis in Paper II.

[15] The log gf values are from Pinnington et al. (1995), Gallagher (1967), and VALD (see Kupka et al. 1999).

Table 2
Log of High-resolution Spectroscopic Observations

Telescope/ Spectrograph (1)	Date (2)	Wavelength Range (Å) (3)	Resolving Power (4)
Magellan/MIKE	2007 Jun 20–23	3300–4900	39000
		4900–9400	31000
	2007 Dec 21–22	3300–4900	37000
		4900–9400	30000
	2008 Sep 6–7	3300–4900	36000
		4900–9400	30000
Keck/HIRES	2007 Nov 30–Dec 1	3720–4600	48000
		4660–5600	48000
		5660–6540	48000
	2008 Mar 25–28	4020–4660	49000
		4750–6190	49000
		6340–7760	49000
VLT/UVES	2008 Jul 3–24	3300–4520	40000
	(2.7 hr Service Observing)	4790–5750	40000
		5840–6800	40000

We have compared our results with those of other workers. Figures 3(b) and (c) compare the present equivalent widths with those of Lai et al. (2008) (CS 30336−049) and Cohen et al. (2004) (HE 1346−0427), for which the rms scatters are 3.0 and 4.4 mÅ, respectively. We have also obtained data for well-observed stars in the present program and found good agreement with the results of others. As an example, Figure 3(d) compares our equivalent widths with those of Cayrel et al. (2004) for CD−38° 245, where the rms scatter is 2.4 mÅ.

3.3. Radial Velocities

Radial velocities were measured from the high-resolution spectra (for all but one program star, HE 1506−0113) using the FXCOR task in IRAF. We cross-correlated individual spectra with a template spectrum obtained with the same setup on the same observing run (generally a high-S/N exposure of a metal-poor standard).[16] Given the weakness of lines in these extremely metal-poor stars, only a limited number of orders provided useful information. In these orders, the peak of the cross-correlation function was fit with a Gaussian. The velocities from multiple orders were averaged to obtain our final radial velocities for each individual spectrum with a typical uncertainty of 0.5 km s^{-1}, but with values as high as 3 km s^{-1}. For HE 1506−0113 the velocity was determined from the four individual Very Large Telescope (VLT) spectra discussed in Section 3.1, by cross-correlating them with a model atmosphere synthetic spectrum as described by Norris et al. (2010b, Section 2.4).

Table 7 presents average heliocentric velocities obtained on each of our observing runs, together in Table 8 with velocities and the epoch of observation for each individual observation.

4. TEMPERATURE AND GRAVITY DETERMINATIONS

In order to determine the stellar atmospheric parameters necessary for our subsequent chemical abundance analysis we have adopted three independent techniques. First, we employed

[16] Our templates were CS 22892−052: 13.1 km s^{-1} (2007 June), BD−18° 5550: −126.2 km s^{-1} (2007 November), BD+9° 2190: 266.1 km s^{-1} (2007 December), BD+9° 2190: 266.1 km s^{-1} (2008 March), and HD140283: −170.4 km s^{-1} (2008 September).

Table 3
Atomic Data and Equivalent Widths (mÅ) for Program Stars

Wavelength (Å)	Species	χ (eV)	loggf	52972−1213−507	53327−2044−515	53436−1996−093	54142−2667−094	BS 16545−089	CS 30336−049	HE 0049−3948	HE 0057−5959	HE 0102−1213
(1)	(2)	(3)	(4)	(5)	(6)	(7)	(8)	(9)	(10)	(11)	(12)	(13)
S/N[a]				28	51	129	47	180	126	149	91	81
W(min) (mÅ)				12	7	6	8	5	6	6	6	5
5889.95	11.0	0.00	0.11	183.0	...	...	...	20.2	70.4	10.6	156.0	...
5895.92	11.0	0.00	−0.19	105.0	17.8	10.9	...	11.6	50.6	12.6	129.0	32.7
3829.36	12.0	2.71	−0.21	93.0	65.4	...	88.7	...	93.6	43.8	86.1	78.5
3832.30	12.0	2.71	0.15	...	...	...	...	...	106.5	...	106.5	...
3838.29	12.0	2.72	0.41	...	...	...	...	...	117.5	...	109.5	...

Notes.
[a] S/N per ∼0.17 Å pixel at 4500 Å.
[b] These lines produce discrepant abundances and are not included in the results reported in Paper II.

(This table is available in its entirety in a machine-readable form in the online journal. A portion is shown here for guidance regarding its form and content.)

Table 4
Atomic Data and Equivalent Widths (mÅ) for Program Stars

Wavelength (Å) (1)	Species (2)	χ (eV) (3)	loggf (4)	HE 0146 −1548 (5)	HE 0207 −1423 (6)	HE 0228 −4047 (7)	HE 0231 −6025 (8)	HE 0253 −1331 (9)	HE 0314 −1739 (10)	HE 0355 −3728 (11)	HE 0945 −1435 (12)	HE 1055 +0104 (13)	HE 1116 −0054 (14)
S/N[a]				34	23	118	42	41	43	29	158	49	128
W(min) (mÅ)				14	13	6	13	10	9	20	5	9	7
5889.95	11.0	0.00	0.11	186.0	138.5	...	44.2	45.1	29.9	...	...	67.1	16.4
5895.92	11.0	0.00	−0.19	154.5	...	...	37.7	23.4	...	...	...	39.6	10.6
3829.36	12.0	2.71	−0.21	...	...	43.2	100.2	88.8	78.4	...	...	98.1	55.0
3832.30	12.0	2.71	0.15	...	...	...	...	...	...	...	...	...	...
3838.29	12.0	2.72	0.41	...	...	...	...	...	...	...	...	...	...

Notes.
[a] S/N per ∼0.17 Å pixel at 4500 Å.
[b] These lines produce discrepant abundances and are not included in the results reported in Paper II.

(This table is available in its entirety in a machine-readable form in the online journal. A portion is shown here for guidance regarding its form and content.)

Table 5
Atomic Data and Equivalent Widths (mÅ) for Program Stars

Wavelength (Å) (1)	Species (2)	χ (eV) (3)	loggf (4)	HE 1142 −1422 (5)	HE 1201 −1512 (6)	HE 1204 −0744 (7)	HE 1207 −3108 (8)	HE 1320 −2952 (9)	HE 1346 −0427 (10)	HE 1402 −0523 (11)	HE 1506 −0113 (12)	HE 2020 −5228 (13)	HE 2032 −5633 (14)
S/N[a]				62	219	27	66	61	206	77	64	37	56
W(min) (mÅ)				15	5	16	10	10	5	8	5	13	10
5889.95	11.0	0.00	0.11	87.9	17.7	67.8	156.0	79.5	19.8	29.7	185.0	...	23.5
5895.92	11.0	0.00	−0.19	53.7	8.5	...	105.0	55.8	13.7	25.9	152.0	...	9.9
3829.36	12.0	2.71	−0.21	139.5	60.7	...	101.8	100.7	...	86.7	138.0	85.5	59.6
3832.30	12.0	2.71	0.15	...	...	...	128.5	123.0	...	...	...	116.5	...
3838.29	12.0	2.72	0.41	...	...	...	143.0	136.5	...	...	...	121.5	...

Notes.
[a] S/N per ∼0.17 Å pixel at 4500 Å.
[b] These lines produce discrepant abundances and are not included in the results reported in Paper II.

(This table is available in its entirety in a machine-readable form in the online journal. A portion is shown here for guidance regarding its form and content.)

Table 6
Atomic Data and Equivalent Widths (mÅ) for Program Stars

Wavelength (Å) (1)	Species (2)	χ (eV) (3)	loggf (4)	HE 2047 −5612 (5)	HE 2135 −1924 (6)	HE 2136 −6030 (7)	HE 2139 −5432 (8)	HE 2141 −0726 (9)	HE 2142 −5656 (10)	HE 2202 −4831 (11)	HE 2246 −2410 (12)	HE 2247 −7400 (13)
S/N[a]				63	75	31	86	44	48	37	61	23
W(min) (mÅ)				10	7	15	8	10	15	15	8	20
5889.95	11.0	0.00	0.11	44.2	17.6	38.7	146.0	45.2	187.0	...	142.0	...
5895.92	11.0	0.00	−0.19	22.2	36.2	24.9	130.0	26.5	166.5	192.5	120.0	170.5
3829.36	12.0	2.71	−0.21	68.7	57.5	70.6	136.0	88.3	166.5	...	85.3	...
3832.30	12.0	2.71	0.15	...	...	120.0	...	...	...	...	...	...
3838.29	12.0	2.72	0.41	...	...	119.0	...	...	...	...	...	...

Notes.
[a] S/N per ∼0.17 Å pixel at 4500 Å.
[b] These lines produce discrepant abundances and are not included in the results reported in Paper II.

(This table is available in its entirety in a machine-readable form in the online journal. A portion is shown here for guidance regarding its form and content.)

the fitting of model atmosphere fluxes to spectrophotometric observations. In principal, this provides unique values of the $T_{\rm eff}$, log g, and metallicity [M/H], although uncertainties in interstellar reddening, flux calibration, and model atmosphere fluxes can influence the fits. The metallicity determined from the global flux is the least precisely determined parameter, but the imprecision little affects fitting the other two parameters. Interstellar reddening is very important because it affects the fitted value of both $T_{\rm eff}$ and log g. In some cases, the reddening can be fitted together with the stellar parameters by comparing the size of the residuals between the different reddening-corrected observations and the fitted fluxes. In other cases, its value can be achieved by examining the variation of the residuals with wavelength. Theoretical isochrones for halo stars can also be used to constrain combinations of $T_{\rm eff}$, log g, [M/H], and $E(B-V)$.

A second important determinant of $T_{\rm eff}$ is the hydrogen line profiles, in particular those of Hα, Hβ, and Hγ. For $T_{\rm eff} <$ 7000 K, the hydrogen line profile wings are only slightly sensitive to log g, but given an estimate of the appropriate

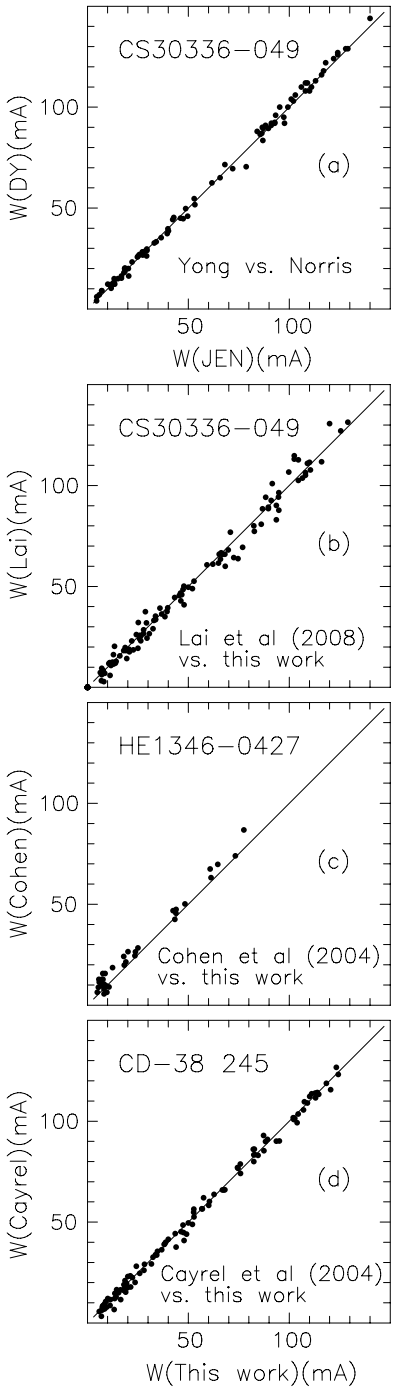

Figure 3. Comparison of equivalent widths (a) measured in the present work by J.E.N. and D.Y., and (b)–(d) between the present work and that of Lai et al. (2008), Cohen et al. (2004), and Cayrel et al. (2004).

Table 7
Radial Velocities

Star	Telescope[a]/Date	V_r[b] (km s^{-1})	s.e.[b] (km s^{-1})
(1)	(2)	(3)	(4)
52972−1213−507	K Nov07	−177.0	0.5
53327−2044−515	K Nov07	−193.5	0.5
53436−1996−093	K Nov07	−15.3	1.7
	K Mar08	−17.2	0.5
54142−2667−094	K Nov07	43.4	0.7
BS 16545−089	K Mar08	−161.1	0.5
CS 30336−049	M Jun07	−236.6	0.8
HE 0049−3948	M Dec07	190.8	0.5
	M Sep08	190.6	0.9
HE 0057−5959	M Jun07	375.3	0.5
HE 0102−1213	K Nov07	90.5	0.5
HE 0146−1548	K Nov07	−114.9	0.5
HE 0207−1423	K Nov07	−209.6	0.5
HE 0228−4047	M Dec07	123.8	0.6
	M Sep08	128.5	1.5
HE 0231−6025	M Dec07	296.6	0.5
HE 0253−1331	K Nov07	25.2	0.5
HE 0314−1739	K Nov07	40.9	0.5
HE 0355−3728	M Dec07	82.0	1.8
HE 0945−1435	K Mar08	121.8	0.5
HE 1055+0104	K Nov07	324.6	0.5
HE 1116−0054	M Jun07	149.1	0.7
	K Nov07	148.3	1.3
	M Dec07	149.3	0.7
	K Mar08	148.3	0.8
HE 1142−1422	M Jun07	−102.3	0.5
HE 1201−1512	M Jun07	238.8	0.5
	K Mar08	237.2	0.5
HE 1204−0744	M Jun07	−49.7	2.7
HE 1207−3108	M Jun07	−3.7	0.5
HE 1320−2952	M Jun07	390.0	0.5
	K Mar08	390.0	0.9
HE 1346−0427	K Mar08	−47.8	0.5
HE 1402−0523	M Jun07	−68.8	0.5
HE 1506−0113	V Jul08	−137.1	0.3
HE 2020−5228	M Jun07	−41.5	2.2
HE 2032−5633	M Jun07	260.5	0.5
HE 2047−5612	M Jun07	−50.0	1.6
HE 2135−1924	K Nov07	−252.9	1.6
HE 2136−6030	M Jun07	156.5	2.8
HE 2139−5432	M Dec07	113.4	0.7
	M Sep08	115.5	0.5
HE 2141−0726	K Nov07	−38.1	0.5
HE 2142−5656	M Jun07	103.4	0.5
HE 2202−4831	M Jun07	56.2	0.5
HE 2246−2410	M Jun07	−3.1	1.8
HE 2247−7400	M Jun07	5.7	0.5

Notes.
[a] K = Keck, M = Magellan, V = VLT.
[b] Heliocentric radial velocity and standard error of the mean.

log g from the flux fitting, an excellent reddening-independent temperature can be derived (e.g., Fuhrmann et al. 1993; Barklem et al. 2002; Asplund et al. 2006; Barklem 2008). Care must be taken to ensure that the continuum of the echelle spectra over the hydrogen lines is correctly defined, but this can be done reliably using a smooth-spectrum star or the shape of the continuum in neighboring orders. The treatment of convection in the one-dimensional model atmospheres does alter the hydrogen line profiles (e.g., Fuhrmann et al. 1993; Barklem et al. 2002; Heiter et al. 2002; Barklem 2008), but these differences are minimal for Hα. More recently, the effects on hydrogen lines of three-dimensional hydrodynamical model atmospheres in self-consistently computed convective energy transport has been explored (e.g., Ludwig et al. 2009), but a systematic study of the observed spectra of three-dimensional models still remains to be done. In the present work we have adopted the one-dimensional formalism, and intend to return to this important issue in a later study.

Finally, we also used an Hδ line index (HP2) measured from medium-dispersion spectra and calibrated as a function of $T_{\rm eff}$ for a large sample of stars (see the Appendix). This is a very

Table 8
Individual Radial Velocities

Star	Telescope[a]/Date	Julian Date	V_r[b] (km s^{-1})
(1)	(2)	(3)	(4)
52972−1213−507	K Nov07	2454437.06233	−176.6
	K Nov07	2454437.07710	−177.3
53327−2044−515	K Nov07	2454435.94873	−193.7
	K Nov07	2454436.81393	−193.1
	K Nov07	2454436.85729	−193.7
53436−1996−093	K Nov07	2454437.09230	−11.0
	K Nov07	2454437.10709	−15.6
	K Nov07	2454437.13194	−16.4
	K Nov07	2454437.14671	−18.0
	K Mar08	2454552.81982	−17.7

Notes.
[a] K = Keck, M = Magellan, V = VLT.
[b] Heliocentric radial velocity.

(This table is available in its entirety in a machine-readable form in the online journal. A portion is shown here for guidance regarding its form and content.)

useful technique, as it is independent of reddening, and can be used when a flux-calibrated spectrum is unavailable.

We discuss each of these in turn.

4.1. Spectrophotometry

The flux spectrum of a star can be considered as reflecting the underlying blackbody temperature, moderated by the photospheric opacity sources. In the UV–optical region for A–K stars, there are two main continuum opacity sources: bound-free neutral hydrogen (b-f H I) and the bound-free negative hydrogen ion (photoelectric ionization) (b-f H^-) (see, e.g., Gray 1992). In the UV below 3646 Å, absorption from H I atoms in level $n = 2$ produces the Balmer continuum. In the optical between 3646 Å and 8206 Å, absorption from H I atoms in level $n = 3$ produces the Paschen continuum. Plotted against wavelength, the shape of the b-f H I opacity is a series of ramps that terminate abruptly at wavelengths corresponding to the different excitation levels of the hydrogen atom. In contrast, the b-f H^- opacity is smooth and approximately bell-shaped (FWHM 10000 Å), with maximum absorption at about 8500 Å. The b-f H I opacity dominates in A stars, while H^- dominates for temperatures cooler than the Sun. As the ratio of the number of H^- to H I is proportional to the electron pressure (or effective gravity), higher gravity increases the contribution of the H^- opacity relative to that from H I.

Figure 4 shows the spectra of three MARCS models with the same $T_{\rm eff}$ and metallicity but different values of $\log g$ corresponding to the halo main sequence, subgiant branch, and horizontal branch. From these spectra one can see how decreasing gravity increases the Balmer Jump (the difference in flux between the Balmer and Paschen continua), and more subtly, makes the slope of the Paschen continuum bluer. It is the interplay between the different contributions made by the H^- and H I opacity for different temperatures and gravities that enables the gravity to be derived (for 4500 K $\lesssim T_{\rm eff} \lesssim$ 9000 K) from fitting the flux-calibrated spectrum (e.g., Barbier & Chalonge 1939; Oke 1965; Bessell 2007).

In fitting the flux spectrum of an F–K star, one should note that the temperature is determined mainly from the slope of the Paschen continuum; however, the strength of the hydrogen lines, which are mainly sensitive to temperature in this spectral-type range, can serve as valuable consistency checks on the adopted reddening and the Paschen continuum slope fit. At medium resolution, the metallicity can also be estimated from individual strong lines, such as Ca II and Mg I, as well as from general metal-line blanketing in the violet, and from the strength of molecular bands, such as CH (for carbon-normal stars), MgH, and TiO. How well all these features are fitted is quantitatively evaluated to determine the spectrophotometrically derived $T_{\rm eff}$, $\log g$, [M/H], and $E(B-V)$. The precision of the spectrophotometrically derived metallicity differs with $T_{\rm eff}$, being higher for K stars than for F stars, but in our experience is normally within ±0.2 dex of the high-resolution spectroscopic estimate. This is more than adequate for discovery programs and for determining $T_{\rm eff}$ and $\log g$ values.

4.1.1. Spectrophotometric Observations

Medium-resolution spectra of our program stars were taken with the ANU's 2.3 m Telescope on Siding Spring Mountain, primarily with the Double Beam Spectrograph (DBS) at 4 Å resolution, together with some at 2 Å resolution with the Wide-Field Integral Field Spectrograph. Both are double-beam spectrographs that use a dichroic mirror to separate the blue (3000–6200 Å) and red (6000–9700 Å) regions. The spectra were taken using a 2 arcsec slit, with the spectrograph orientation set so the atmospheric dispersion was along the slit. Spectrophotometric standards were also observed each night, together with a smooth-spectrum star to enable the removal of telluric features (e.g., Bessell 1999). We used an updated list of standards (available from http://www.mso.anu.edu.au/∼bessell/FTP/Spectrophotometry/) that were selected from the Next Generation Spectral Library (Heap & Lindler 2007, http://archive.stsci.edu/prepds/stisngsl/index.html).

The CCD frames were bias subtracted and flat fielded, the cosmic rays removed, the star and sky spectra extracted, and the sky removed. All spectra were divided by the extracted spectrum of a smooth-spectrum star (generally EG131 or L745-46a, cool He white dwarfs) to remove the signatures of the grating and CCD response, and in the red, any telluric absorption, resulting in a gently curved spectrum. The spectra were then wavelength fitted, wavelength scrunched (rebinned to a linear scale), and corrected for the continuous atmospheric extinction appropriate for their observed airmass. The standard-star spectra (generally 8–10 per night) were compared with their standard values, and the mean spectrophotometric calibration determined and applied to all the program stars.

4.1.2. Model Atmosphere Fluxes

We initially used the Munari et al. (2005, http://archives.pd.astro.it/2500-10500/) library of synthetic spectra at 1 Å resolution, but have recently added the LTE model atmosphere fluxes from the MARCS grid (Gustafsson et al. 2008, http://marcs.astro.uu.se). The MARCS spectra are not line-by-line computed spectra (as are the Munari et al. spectra), but are fluxes generated using statistically sampled opacities; however, smoothed to 4 Å resolution they are very good representations of real spectra. Although restricted to temperatures below 8000 K, the MARCS model atmosphere grid covers all the parameter space of the halo stars that we are interested in.

The Munari et al. (2005) spectra cover a wide range of atmospheric parameters: 3500 K $< T_{\rm eff} <$ 47,500 K, 0.0 $< \log g <$ 5.0, and −2.5 $<$ [M/H] $<$ +0.5. Extension of the full grid to lower metallicity is underway by R. Sordo (2010, private communication), but many

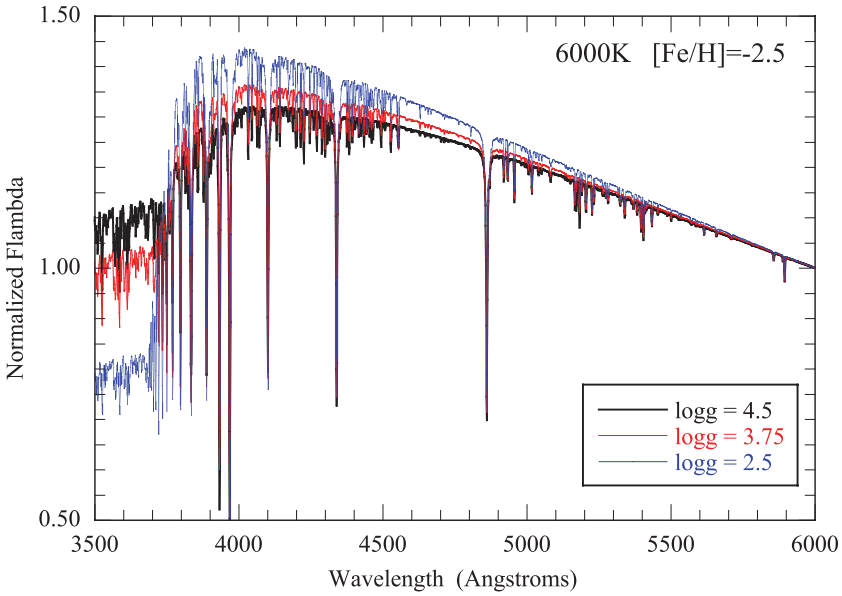

Figure 4. Spectrum of three MARCS models with the same $T_{\rm eff}$ = 6000 K and metallicity [Fe/H] = −2.5 but different values of log g corresponding to the main sequence, subgiant branch, and horizontal branch for halo stars. Note not only the different Balmer Jumps, but the different slopes redward of the Balmer Jump.
(A color version of this figure is available in the online journal.)

relevant lower metallicity models are already available from http://www.user.oat.ts.astro.it/castelli/spectra.html.

For the MARCS spectra, the stellar atmospheric model parameters ranged in $T_{\rm eff}$ from 2500 K to 8000 K, in steps of 100 K from 2500 K to 4000 K, and in steps of 250 K between 4000 K and 8000 K. The log g values were between −1.0 and 5.5 in steps of 0.5. Overall logarithmic metallicities relative to the Sun were between −5.0 and +1.0 in variable steps. The reference solar abundance mixture was that of Grevesse et al. (2007). Plane-parallel models were used for gravities between 3.0 and 5.0, and spherical models (1 $M_{\odot}$) for lower gravities. For the lower-metallicity stars, alpha-enhanced models were used: $[\alpha/{\rm Fe}] = +0.25$, for $-0.5 \leqslant {\rm [Fe/H]} \leqslant -1.5$, and +0.50, for $-1.5 < {\rm [Fe/H]} \leqslant -5.0$.

4.1.3. Spectrophotometric Flux Fitting Method

A *python* (http://www.python.org/psf) program, *fitter*, written by S.J.M., was used for the fitting. This will be described in greater detail in a later paper, together with parameters for many more stars. Basically, the grid of fluxes was initially interpolated to produce a new grid at spacings of 100 K in $T_{\rm eff}$, 0.5 in log g, and 0.1 in [M/H]. The software was run using parallel-processing architecture, with each of the 25 processors allocated model spectra for a single metallicity.

The model fluxes were smoothed to a resolution similar to that of the observations and the observed fluxes and the model fluxes renormalized to the mean flux between 4500 and 5500 Å. The radial velocity of the observed star was obtained through cross-correlation of deep lines with a model spectrum, and the observed spectrum shifted to match the model. We were also able to mask out regions of the observed spectrum that we wish to ignore in the fitting, such as the regions around the CH and C_2 bands in C-rich stars. Each model spectrum in the new grid was then cross-correlated against the observed spectrum, the rms of the fit computed and the parameters of the best-fitting grid spectrum identified. A new grid centered on these parameters was then interpolated at a finer spacing of 25 K in $T_{\rm eff}$ and 0.1 dex in log g, and these finer-spaced grid spectra were cross-correlated against the observed spectrum, the rms of the fit calculated, and the best-fitting parameters again selected. Fitting only the blue spectrum was found to be adequate for most halo stars, but we did fit the combined blue and red spectrum from 3600 Å to 9000 Å. Figure 5 shows the result of one such fit for the blue spectrum of the metal-poor star HE 1311−0131, using the MARCS grid.[17]

Revised fits of fluxes corrected for interstellar reddening corresponding to a single value, or a range of $E(B-V)$ values, can also be assessed. The reddening curve used is from Mathis (1990). To assist in estimating the reddening, the Schlegel et al. (1998) reddening (maximum possible value in that direction) is indicated on the output for each star. It was also noted that there is strong evidence for a reddening-free bubble within 100 pc of the Sun (e.g., Frisch et al. 2011; Abt 2011) that likely extends even farther in the directions of the Galactic poles. It should also be kept in mind that the continuum temperatures derived with no reddening are minimum temperatures, as any corrections for reddening will increase the fitted temperatures. The spectrophotometrically derived $T_{\rm eff}$, log g, and $E(B-V)$ are given in Columns 2–4 of Table 9. We choose not to list the derived [M/H] value, but defer to the precisely determined values in Paper II.

4.2. Hα, Hβ, and Hγ Line Profile Fitting

In F, G, and K stars, where the negative hydrogen ion is the dominant source of continuous opacity, hydrogen Balmer-line wings are extremely useful indicators of $T_{\rm eff}$, since their strength is, to a large degree, independent of other parameters such as hydrogen abundance, gravity, and chemical composition (e.g., Fuhrmann et al. 1993). Barklem (2008) discusses the pros and cons in the use of hydrogen Balmer lines

[17] We have not used the wavelength region 3700–3900 Å, which includes the confluence of the Balmer series, since experience shows this detracts from the goodness of fit we obtain for the Balmer discontinuity. When spectra of carbon-rich stars with obviously strong CH and/or C_2 bands were fitted with scaled solar metallicity model atmosphere fluxes, the CH and C_2 bands were masked out in the fit.

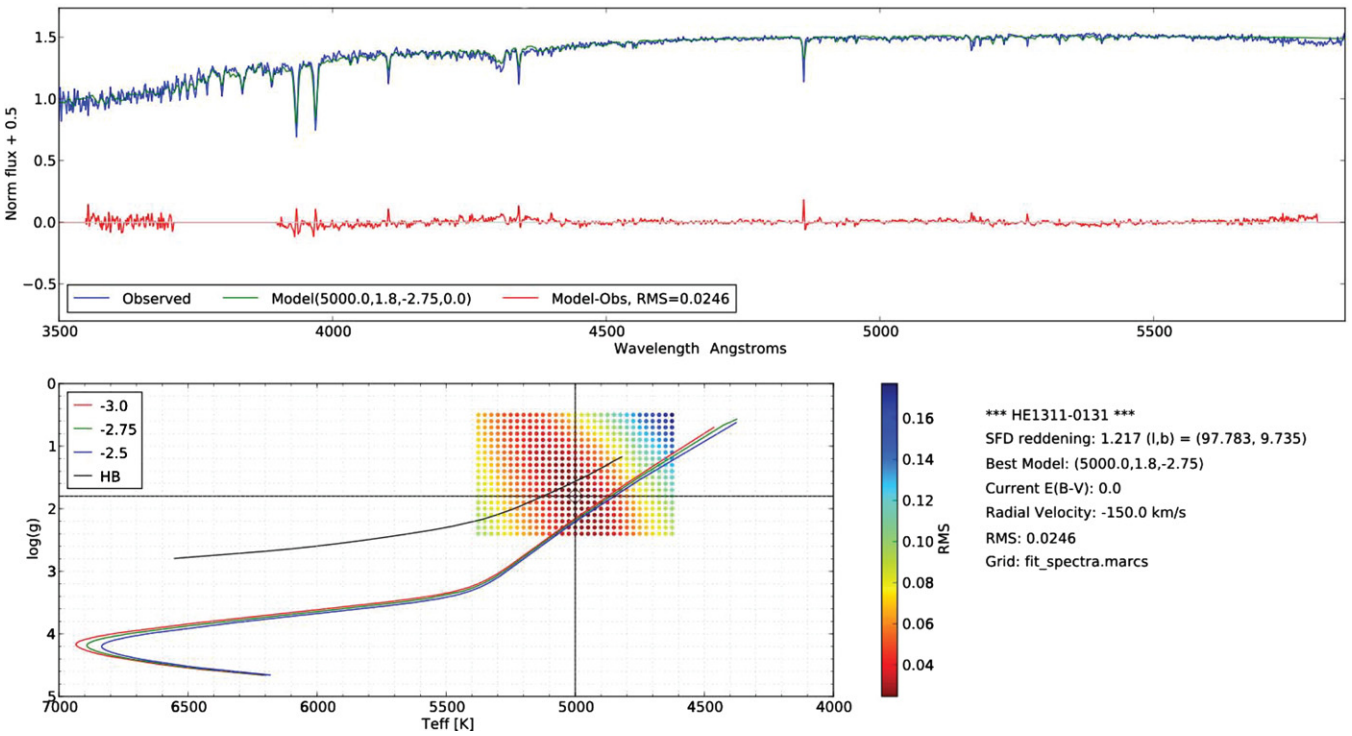

Figure 5. Output of *fitter*. In the top frame the blue line represents the observed spectrum, the green line is the best-fitting model spectrum, and the red line is the difference spectrum. In the lower frame, the cross-hair marks the best-fitting $T_{\rm eff}$ and $\log g$ and the rms values of the fits are represented in color for the small subgrid about the initial best-fitting parameters. The rms–color palette is shown ranging from black for best to blue for worst. Any combination of parameters within the black shaded region is acceptable. The halo isochrones are drawn to assist the selection of the most likely parameters.

as high-precision diagnostics of effective temperature in these stars, and highlights the improvements in detectors and broadening theory that underpin this. Barklem & Piskunov (2003) detail publicly available codes that can be used to compute Balmer-line profiles, and include the advances in broadening theory. However, Barklem (2008) notes the role of possible departures from LTE, differences between one-dimensional and three-dimensional model atmospheres, and the effects that the value of the mixing-length parameter has on the Balmer-line profiles.

The $T_{\rm eff}$ were derived by P.S.B. from fitting the Hα, Hβ, and Hγ profiles measured from our echelle spectra[18] described in Section 3.1. The method employed for merging of spectral orders and continuum normalization of the spectra and subsequent analysis follows precisely that described in Barklem et al. (2002). The most important aspects of the analysis are as follows. Synthetic profiles are computed assuming LTE line formation using one-dimensional LTE plane-parallel MARCS models (Asplund et al. 1997), with convection described by mixing-length theory with parameters $\alpha = 0.5$ and $y = 0.5$. The most important line-broadening mechanisms for the wings are Stark broadening and self-broadening, which are described by calculations of Stehlé & Hutcheon (1999) and Barklem et al. (2000), respectively. The fitting is done by minimization of the χ^2 statistic, comparing the observed and synthetic profiles in spectral windows believed to be free of blends in the solar spectrum. To illustrate the fitting method and the temperature sensitivity of the hydrogen line profiles, Figure 6 shows fits to Hα, Hβ, and Hγ line profiles for HE 2047−5612, a typical halo subgiant.

[18] We chose not to analyze Hδ because of its lower S/N on our spectra, which affects both local fitting and the ability to reliably apply the continuum normalization techniques used here.

The choice to use LTE analysis follows the reasoning presented in Aoki et al. (2009) and bears repeating here. The assumption of LTE for the line wings has been shown to be questionable on the basis of theoretical non-LTE calculations (Barklem 2007), the role of hydrogen collisions being a major uncertainty. Those calculations suggest that the temperatures from LTE Balmer-line wings could be systematically too cool, by of the order of 100 K if hydrogen collisions are inefficient, although if collisions are efficient, LTE is not ruled out. Since there is no strong evidence favoring any particular hydrogen collision model, we calculate in LTE, as this temperature scale is well studied, and it is computationally most practical. However, we emphasize that LTE is not a safe middle ground, and will lead to temperatures that are systematically too cool, should departures from LTE exist in reality.

The individual Balmer lines have distinct characteristics and behaviors; so, as in Aoki et al. (2009), we chose not to give $T_{\rm eff}$ from all lines equal weight in determining our final Balmer-line $T_{\rm eff}$. Hα is often preferred over other lines in solar-type stars, for the reasons discussed by Fuhrmann et al. (1993). However, in metal-poor stars it is not clear that Hα is to be preferred. Blending by metal lines becomes unimportant, and Hβ becomes insensitive to gravity, while Hα is quite gravity sensitive (see Barklem et al. 2002, their Table 4) and rather insensitive to $T_{\rm eff}$ (see Figure 6). These differences in behavior arise due to changes in the relative importance of Stark and self-broadening. Moreover, the calculations by Barklem (2007) suggest that non-LTE effects, if they exist, will be largest in Hα. Hγ, while having similar sensitivities to Hβ, is generally not as reliable as Hβ. This is predominantly due to increased blending in this region of the spectrum, especially in CEMP stars with strong *G* bands, which affects both the local fitting of the line and nearby orders used to define the continuum placement. In addition, the

Table 9
$T_{\rm eff}$, log g, $E(B-V)$, and HP2 for Program Stars

Star	$T_{\rm eff}$[a] (K)	log g[a]	$E(B-V)$[a] mag	$T_{\rm eff}$[b] (K)	$\sigma(T_{\rm eff})$[b] (K)	No. of[b] H lines	log g[b]	HP2 (Å)	$T_{\rm eff}$[c] (K)	$T_{\rm eff}$ (K)	s.e.($T_{\rm eff}$) (K)
(1)	(2)	(3)	(4)	(5)	(6)	(7)	(8)	(9)	(10)	(11)	(12)
52972−1213−507[d]	...	...	...	6463	149	2	4.50	...	...	6463	...
53327−2044−515	5650	3.50	0.14	5640	85	2	4.50	2.74	5820	5703	58
53436−1996−093	...	...	...	6442	12	5	4.30	4.57	6455	6449	6
54142−2667−094	6475	4.10	0.03	6460	21	2	3.90	4.48	6434	6456	11
BS 16545−089	6625	4.00	0.00	6347	40	3	3.80	...	...	6486	139
CS 30336−049	4800	2.40	0.05	4562	67	3	1.50	1.03	4812	4725	81
HE 0049−3948	6500	4.10	0.00	6357	75	3	3.80	5.02	6542	6466	55
HE 0057−5959	5375	3.30	0.00	5230	61	3	2.40	1.56	5167	5257	61
HE 0102−1213	6100	3.80	0.03	5886	35	2	3.80	4.03	6314	6100	123
HE 0146−1548[d]	4775	1.70	0.00	4496	57	2	1.20	...	...	4636	139
HE 0207−1423[d]	5125	2.40	0.00	4920	0	1	1.80	...	...	5023	102
HE 0228−4047	6575	4.30	0.02	6362	87	3	3.70	5.55	6609	6515	77
HE 0231−6025	6500	4.10	0.00	6265	35	3	4.20	5.04	6545	6437	86
HE 0253−1331	6500	4.10	0.02	6393	7	2	4.50	4.95	6530	6474	41
HE 0314−1739	6625	4.40	0.04	6563	7	2	4.30	4.90	6521	6570	30
HE 0355−3728	6450	4.20	0.01	6385	35	3	3.90	...	...	6418	32
HE 0945−1435	6325	4.40	0.04	6285	53	3	3.60	4.43	6421	6344	40
HE 1055+0104	6375	4.30	0.03	6120	42	2	3.80	4.21	6365	6287	83
HE 1116−0054	6550	4.30	0.07	6391	20	11	3.70	4.43	6420	6454	48
HE 1142−1422	6275	2.80	0.06	6083	71	3	2.60	4.18	6356	6238	80
HE 1201−1512	5850	4.20	0.03	5653	125	6	4.50	2.45	5672	5725	62
HE 1204−0744	6525	4.10	0.05	6442	87	3	4.40	5.01	6534	6500	29
HE 1207−3108	5300	2.60	0.01	5382	60	3	3.10	1.61	5199	5294	52
HE 1320−2952	5070	2.40	0.04	5258	44	6	2.00	1.29	4989	5106	79
HE 1346−0427	6325	4.40	0.00	6185	81	3	3.80	...	...	6255	70
HE 1402−0523	6425	4.20	0.02	6350	38	3	3.80	4.68	6479	6418	37
HE 1506−0113[d]	5075	2.40	0.05	4957	40	3	2.20	...	...	5016	59
HE 2020−5228	6325	4.00	0.03	6107	40	3	3.80	4.70	6482	6305	108
HE 2032−5633	6525	4.10	0.05	6250	180	3	3.70	5.42	6596	6457	105
HE 2047−5612	6250	4.00	0.05	6040	31	3	3.60	3.39	6095	6128	62
HE 2135−1924	6525	4.40	0.03	6376	57	2	4.50	4.54	6447	6449	43
HE 2136−6030	6450	4.00	0.00	6367	123	3	3.80	...	...	6409	41
HE 2139−5432[d]	5375	2.20	0.01	5457	44	3	2.00	...	...	5416	41
HE 2141−0726	6575	4.40	0.03	6563	78	2	4.20	4.86	6515	6551	18
HE 2142−5656[d]	4975	2.00	0.04	4902	139	3	1.60	...	...	4939	36
HE 2202−4831[d]	5375	2.40	0.00	5287	85	3	2.20	...	...	5331	44
HE 2246−2410	6550	4.20	0.01	6252	164	3	4.50	4.74	6490	6431	90
HE 2247−7400[d]	4875	2.00	0.01	4782	40	3	1.60	...	...	4829	46

Notes.
[a] From fit to spectrophotometric flux.
[b] From fit to Hα, Hβ, and Hγ profiles.
[c] From empirically calibrated Hδ index (HP2). See the Appendix.
[d] C-rich star.

S/N is generally much lower at Hγ due to less flux in the blue. Considering all these factors, we judge Hβ as the most reliable line for determining $T_{\rm eff}$, and so in combining the temperatures from Hα, Hβ, and Hγ, we have given Hβ double weight.

Thus, having determined $T_{\rm eff}$ from each line for each spectrum ($T_{\rm eff}$(Hα), $T_{\rm eff}$(Hβ), $T_{\rm eff}$(Hγ)), to determine the final hydrogen line profile $T_{\rm eff}$(Balmer) for a star we employed the following procedure. For stars with multiple spectra, we first determined the mean $T_{\rm eff}$(Hα), $T_{\rm eff}$(Hβ), $T_{\rm eff}$(Hγ) for the star, weighting each determination by the S/N of the spectra. Next, we combined the mean $T_{\rm eff}$(Hα), mean $T_{\rm eff}$(Hβ), and mean $T_{\rm eff}$(Hγ) temperatures using the 1:2:1 weighting into a final average $T_{\rm eff}$(Balmer). Because the profiles are slightly dependent on the value of log g, where the gravity adopted for the hydrogen line fits differed grossly from that derived from fitting the blue fluxes, the spectrophotometric gravity was used and the hydrogen lines were refitted to obtain a second temperature estimate. In such cases, where multiple analyses were performed with different log g, the standard deviation of the mean $T_{\rm eff}$(Hα), $T_{\rm eff}$(Hβ), and $T_{\rm eff}$(Hγ) values was calculated, and we selected $T_{\rm eff}$(Balmer) as the one with the smallest dispersion. Conversely, where the temperature derived from the hydrogen lines grossly exceeded the continuum-fitted temperature, the application of additional reddening was tested to see whether a higher temperature would give an acceptable fit. The final hydrogen line profile temperatures, $T_{\rm eff}$(Balmer), are given in Column 5 of Table 9, together with the standard deviation, $\sigma(T_{\rm eff})$, of the different hydrogen lines (Column 6) and the number of individual hydrogen line observations used (Column 7). The adopted gravity is given in Column 8.

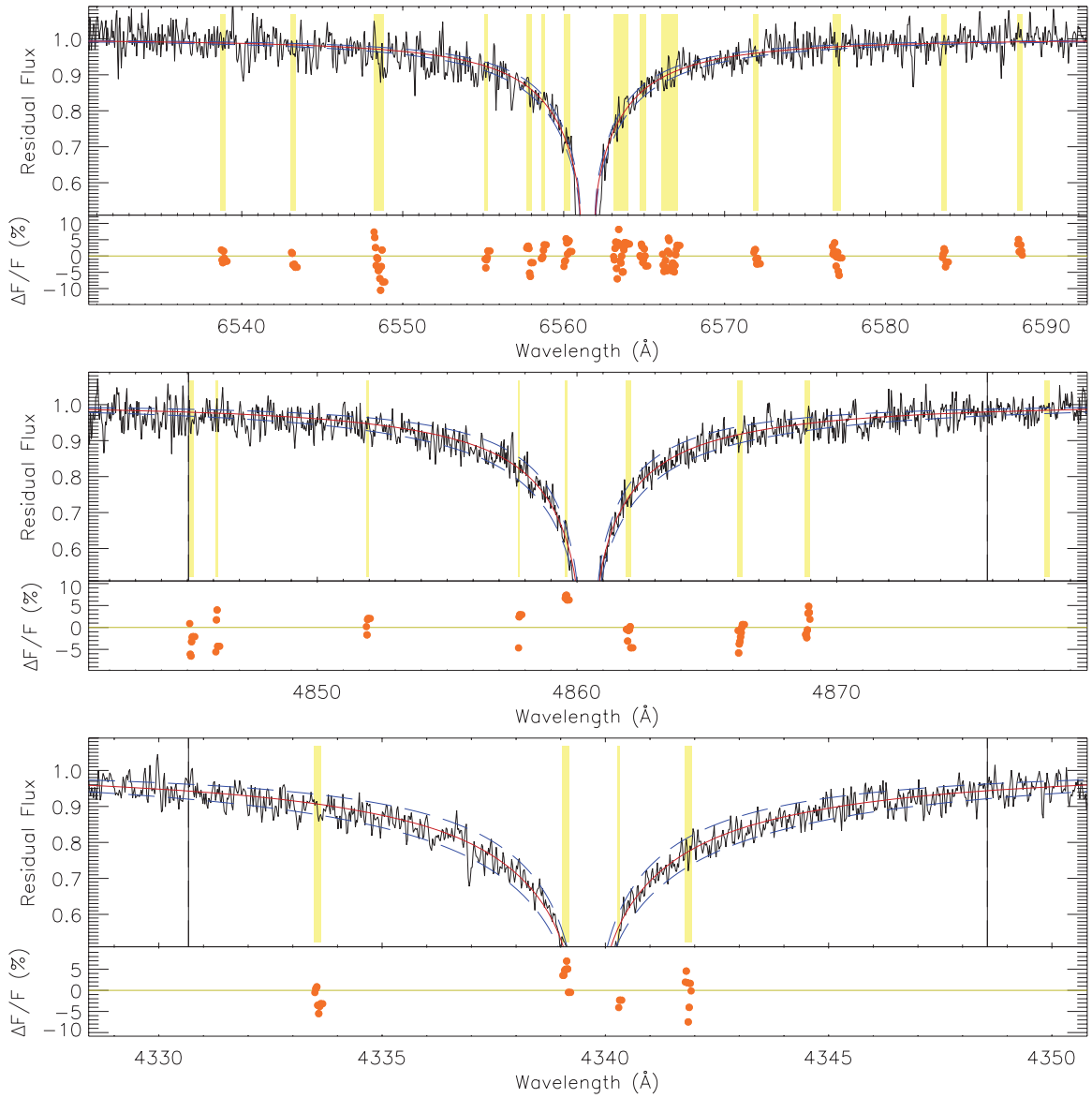

Figure 6. Fits to Hα, Hβ, and Hγ line profiles for HE 2047−5612, $T_{\rm eff}$(Balmer) = 6040 K, assuming log g = 3.6 and [Fe/H] = −3.2. The (black) full lines showing noise are the normalized observed spectra and the (red) smooth full lines the best-fit synthetic profile (corresponding to $T_{\rm eff}$ = 6040, 6020, 6080 K for each line, respectively). The (blue) dashed lines show the synthetic spectra calculated with models 200 K cooler and hotter than the best fit. The (yellow) shaded regions show the windows used for determining the χ^2 statistic in the fitting, the residuals for which are shown directly below in the bottom panel. The full vertical lines show the estimated limit of validity of the impact approximation in the self-broadening calculations, which is beyond the limit of the plot for Hα. Note that the windows outside this region are rejected in the fitting, and thus no residual is plotted.

(A color version of this figure is available in the online journal.)

4.3. Medium-resolution Hδ Index HP2

A third, independent, temperature estimate was obtained from medium-resolution spectroscopy of the Hδ line index (HP2), calibrated as a function of $T_{\rm eff}$ as described in the Appendix. We determined HP2 from the medium-resolution spectra of the candidate most metal-poor stars we observed with the 2.3 m/DBS combination, and those we obtained from the SDSS Data Release 7, as described in Section 2. We now use the above calibration to estimate their effective temperatures, excluding two categories of objects. First, while our calibration may be applied with confidence for "normal" metal-poor stars, it would be inappropriate to use it for carbon-rich objects, because of CH absorption in the bandpasses used to measure HP2. We thus do not present temperatures for the seven objects in our program sample that exhibit strong *G* bands: specifically, we exclude C-rich stars for which the Beers et al. (1999) *G*-band index G′ is larger than ∼1.0 Å (see Table 1). Second, we also exclude stars with fewer than 400 counts/1 Å pixel at 4100 Å, in an effort to exclude objects for which the poorer S/N might be expected to decrease the accuracy of the temperature estimate. The values of HP2 and the inferred values of $T_{\rm eff}$ for the remaining 26 C-normal stars in our most metal-poor star sample are presented in Columns 9 and 10 of Table 9.

4.4. Possible Systematic Differences in Temperature between Techniques

Figure 7 plots the differences between the temperature derived from fitting the overall flux and the temperatures derived from high-resolution hydrogen line profile fitting and the Hδ index. There are indications of some systematic differences in these

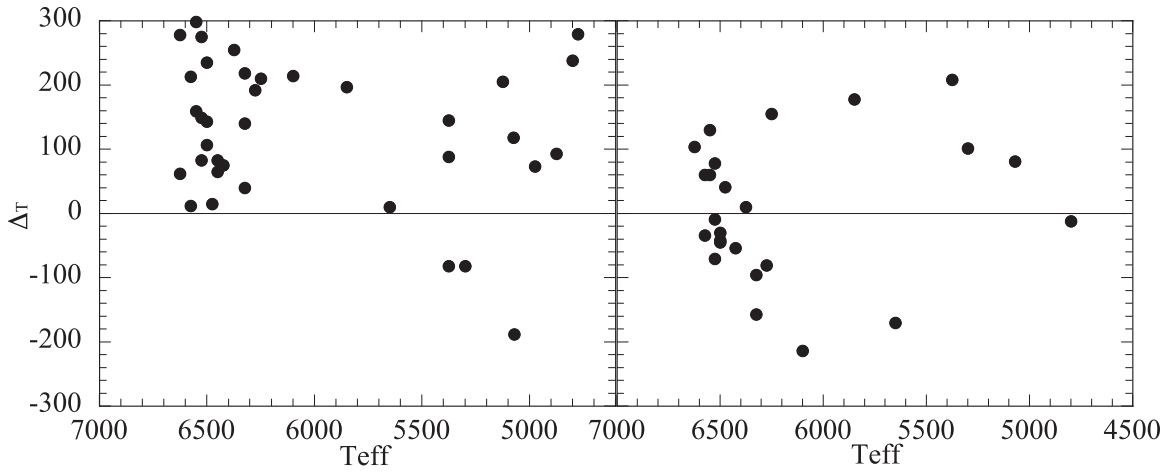

Figure 7. Differences between the $T_{\rm eff}$ derived from flux fitting and those derived from Hα, Hβ, and Hγ profiles (left), and the medium-resolution Hδ index, HP2 (right).

figures. Compared to the temperatures derived from fitting the fluxes, the hydrogen line profiles yielded lower temperatures by 128 ± 18 K (36 stars), while the Hδ index yielded temperatures lower by 8 ± 22 K (25 stars).

As mentioned earlier, the temperatures derived from the hydrogen line profiles may be affected by the neglect of non-LTE and by remaining uncertainties in the broadening theory. The temperatures from flux fitting and hydrogen line fitting may both be affected by the use of one-dimensional model atmospheres rather than three-dimensional model atmospheres, but three-dimensional effects are more likely for the hydrogen lines than the stellar energy distributions (Asplund 2005). We also note that the temperatures from flux fitting are in agreement with those from the infrared flux method for those metal-poor stars in common. Future work by P.S.B. and M.A. is proposed to ascertain the reason or reasons for the cooler hydrogen line temperatures. There is an insignificant difference between the mean flux temperature and the empirically calibrated mean Hδ index temperature.

In the absence of compelling reasons for discounting any of the temperature derivation techniques, we have taken a mean of the derived temperatures to use for our high-resolution abundance analysis (Paper II), but note that these mean temperatures may be ≈50 K cooler than the infrared flux method temperature scale. Our final $T_{\rm eff}$ and their standard error of the mean are presented in Columns 11 and 12 of Table 9.

While spectrophotometry, in principle, remains the best way of obtaining stellar parameters, modern wide-field broadband multicolor surveys such as SDSS, and in particular SkyMapper (Keller et al. 2007), will provide precise photometric indices that can be calibrated using synthetic photometry from model atmosphere fluxes to provide accurate temperatures, and good estimates of gravity and metallicity. Interstellar reddening, however, remains an issue for all photometric techniques, emphasizing the continuing necessity of hydrogen line fitting and the importance of further theoretical work on the formation of hydrogen lines in cool stars.

5. SUMMARY

We report the discovery of 34 stars in the Hamburg/ESO Survey for metal-poor stars and the SDSS that have [Fe/H] $\lesssim -3.0$. Ten of them are newly discovered objects having [Fe/H] < -3.5. We have obtained high-resolution, high-S/N spectra of them and four other extremely metal-poor stars (three of which have [Fe/H] < -3.5), and present equivalent widths and radial velocities for this sample.

$T_{\rm eff}$ has been determined for these objects, employing three independent techniques. First, we analyzed medium-resolution spectra to obtain absolute fluxes. These were fit using model atmosphere fluxes to provide spectrophotometric $T_{\rm eff}$ and log g, with approximate [M/H] and reddening. Second, we fit the wings of the Hα, Hβ, and Hγ lines, measured from our echelle spectra, to model atmosphere line profiles. Although there are some caveats concerning our understanding of the formation of these lines, this technique provides a reliable and reddening-independent method of temperature determination. Finally, we used the observed Hδ index, HP2, together with a calibration of HP2 as a function of $T_{\rm eff}$, for a set of stars that have well-established temperatures, to obtain a third $T_{\rm eff}$ estimate.

There are possible systematic differences in the temperatures derived using these three techniques, of the order of 100 K, and future work is needed to clarify the origin of these differences. Nevertheless, for our purposes, we adopted the average of the three determinations. The mean (internal) error of the resulting temperatures is 63 K, with a dispersion of 33 K.

The data presented here have been analyzed in Papers II, III, and IV of this series (Yong et al. 2013a, 2013b, and Norris et al. 2013, respectively), which includes a homogeneous re-analysis of similar data available in the literature. This has yielded relative chemical abundances for a total of ∼86 stars having [Fe/H] $\lesssim -3.0$ (and some 32 with [Fe/H] $\lesssim -3.5$), which have been used to further constrain the conditions that existed at the earliest times.

J.E.N., M.S.B., D.Y., and M.A. gratefully acknowledge support from the Australian Research Council (grants DP03042613, DP0663562, DP0984924, and FL110100012) for studies of the Galaxy's most metal-poor stars and ultra-faint satellite systems. J.E.N. and D.Y. acknowledge financial support from the Access to Major Research Facilities Program, under the International Science Linkages Program of the Australian Federal Government. Australian access to the Magellan Telescopes was supported through the Major National Research Facilities program. Observations with the Keck Telescope were made under Gemini exchange time programs GN-2007B-C-20 and GN-2008A-C-6. N.C. acknowledges financial support for this work through the Global Networks program of

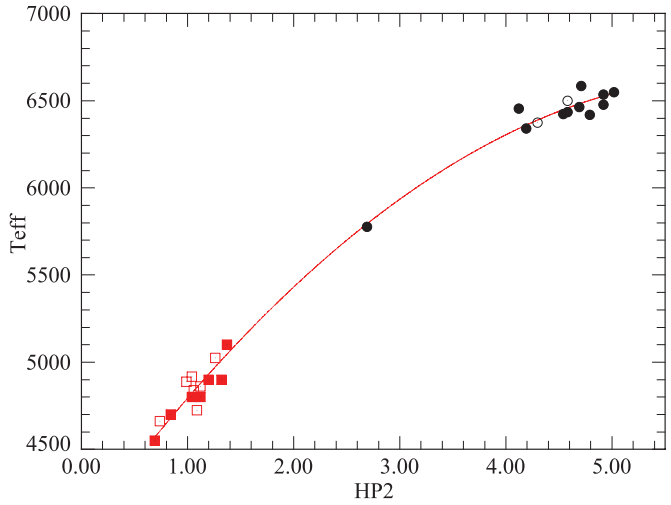

Figure 8. $T_{\rm eff}$ vs. HP2 for calibrating stars. Filled black circles represent dwarfs (and one subgiant) from Casagrande et al. (2010); open black circles are dwarfs from the present work; filled red boxes are giants from Cayrel et al. (2004); and open red boxes are the average values for giants from Cayrel et al. (2004) and the present work. The red line is the fitted quadratic relation.

(A color version of this figure is available in the online journal.)

Universität Heidelberg and Sonderforschungsbereich SFB 881 "The Milky Way System" (subproject A4) of the German Research Foundation (DFG). P.S.B acknowledges support from the Royal Swedish Academy of Sciences and the Swedish Research Council; he is a Royal Swedish Academy of Sciences Research Fellow supported by a grant from the Knut and Alice Wallenberg Foundation. T.C.B. acknowledges partial funding of this work from grants PHY 02-16783 and PHY 08-22648: Physics Frontier Center/Joint Institute for Nuclear Astrophysics (JINA), awarded by the U.S. National Science Foundation. The authors wish to recognize and acknowledge the very significant cultural role and reverence that the summit of Mauna Kea has always had within the indigenous Hawaiian community. We are most fortunate to have the opportunity to conduct observations from this mountain. Finally, we are pleased to acknowledge support from the European Southern Observatory's Director's Discretionary Time Program.

Facilities: ATT(DBS), Keck:I(HIRES), Magellan:Clay (MIKE), VLT:Kueyen(UVES)

APPENDIX

A.1. $T_{\rm eff}$ Calibration of the Hδ Index HP2

A very useful effective temperature estimate for metal-poor stars can be obtained from medium-resolution spectroscopy of the Hδ line index (HP2) calibrated as a function of $T_{\rm eff}$, following Ryan et al. (1999). We used spectra of metal-poor dwarfs and giants that covered the region around Hδ, obtained with ANU's 2.3 m Telescope/Double Beam Spectrograph (DBS) combination on Siding Spring Mountain, as described in Section 2.1 for our observations of candidate most metal-poor stars. The sample comprised 27 stars with abundances in the range $-4.0 <$ [Fe/H] < -2.5 for which temperatures had been determined using a combination of three independent techniques. First, results for 11 dwarfs and subgiants with $T_{\rm eff}$ in the range 5800–6600 K, have been taken from the work of Casagrande et al. (2010), who used the infrared flux method. Second, 14 metal-poor red giants having 4650 K $< T_{\rm eff} <$ 5100 K came from Cayrel et al. (2004, their Table 4), who base their temperatures on calibrations of broadband $B-V$, $V-R$, $V-K$, and $V-I$ photometry. Finally, results for nine dwarfs and giants were determined by M.S.B. for the present work using the spectrophotometric techniques described in Section 4.1. From the DBS spectra, we measured the Hδ index, HP2, of Beers et al. (1999, their Section 3.1.1). The data for our calibration stars are presented in Table 10, where Columns 1–4 contain identification, HP2, $T_{\rm eff}$, and sources, respectively. It is noted here, for completeness, that for the seven red giants with two determinations of $T_{\rm eff}$ the absolute mean difference was 5 K with dispersion 56 K. The calibration data are plotted in Figure 8 together with the fitted quadratic relationship $T_{\rm eff} = 4018. + 842.6 \times {\rm HP2} - 67.70 \times {\rm HP2}^2$, about which the rms deviation is 64 K.

Table 10
Hδ Indices and $T_{\rm eff}$ for Calibration Stars

Star	HP2 (Å)	$T_{\rm eff}$ (K)	Source[a]
(1)	(2)	(3)	(4)
BD +3 740	4.79	6419	1
BD +9 2190	4.92	6477	1
BD +26 3578	4.54	6425	1
BD −13 3442	4.58	6434	1
CD −24 17504	4.12	6455	1
CD −33 1173	5.02	6548	1
CD −38 245	1.12	4800	2
BS 16477−003	1.32	4900	2
CS 22169−035	0.74	4662	2,3
CS 22172−002	1.06	4838	2,3
CS 22186−025	1.20	4900	2
CS 22189−009	0.99	4887	2,3
CS 22873−166	0.69	4550	2
CS 22885−096	1.26	5025	2,3
CS 22891−209	1.09	4725	2,3
CS 22897−008	1.04	4918	2,3
CS 22952−015	1.04	4800	2
CS 22953−003	1.37	5100	2
CS 22968−014	1.12	4862	2,3
CS 29491−053	0.84	4700	2
G 4−37	4.19	6340	1
G 64−12	4.69	6464	1
G 64−37	4.71	6584	1
G 186−26	4.30	6375	3
HD 140283	2.69	5777	1
LP 651−4	4.58	6500	3
LP 815−43	4.92	6535	1

Notes. [a] $T_{\rm eff}$ sources: 1 = Casagrande et al. (2010); 2 = Cayrel et al. (2004); and 3 = Present work.

REFERENCES

Abt, H. A. 2011, AJ, 141, 165
Aoki, W., Barklem, P. S., Beers, T. C., et al. 2009, ApJ, 698, 1803
Aoki, W., Frebel, A., Christlieb, N., et al. 2006, ApJ, 639, 897
Aoki, W., Norris, J. E., Ryan, S. G., Beers, T. C., & Ando, H. 2002, ApJ, 576, L141
Asplund, M. 2005, ARA&A, 43, 481
Asplund, M., Gustafsson, B., Kiselman, D., & Eriksson, K. 1997, A&A, 318, 521
Asplund, M., Lambert, D. L., Nissen, P. E., Primas, F., & Smith, V. V. 2006, ApJ, 644, 229
Barbier, D., & Chalonge, D. 1939, Ann. d'Astrophys., 2, 254
Barklem, P. S. 2007, A&A, 466, 327
Barklem, P. S. 2008, PhST, 133, 014023

Barklem, P. S., & Piskunov, N. 2003, in IAU Symp. 210, Modelling of Stellar Atmospheres, ed. N. Piskunov, W. W. Weiss, & D. F. Gray (Cambridge: Cambridge Univ. Press), E28
Barklem, P. S., Piskunov, N., & O'Mara, B. J. 2000, A&A, 363, 1091
Barklem, P. S., Stempels, H. C., Allende Prieto, C., et al. 2002, A&A, 385, 951
Beers, T. C., & Christlieb, N. 2005, ARA&A, 43, 531
Beers, T. C., Preston, G. W., & Shectman, S. A. 1985, AJ, 90, 2089
Beers, T. C., Preston, G. W., & Shectman, S. A. 1992, AJ, 103, 1987
Beers, T. C., Rossi, S., Norris, J. E., Ryan, S. G., & Shefler, T. 1999, AJ, 117, 981
Bessell, M. S. 1999, PASP, 111, 1426
Bessell, M. S. 2007, PASP, 119, 605
Bessell, M. S., & Norris, J. E. 1984, ApJ, 285, 622
Caffau, E., Bonifacio, P., François, P., et al. 2011, Natur, 477, 67
Carney, B. W., Latham, D. W., Laird, J. B., & Aguilar, L. A. 1994, AJ, 107, 2240
Casagrande, L., Ramírez, I., Meléndez, J., Bessell, M., & Asplund, M. 2010, A&A, 512, A54
Cayrel, R., Depagne, E., Spite, M., et al. 2004, A&A, 416, 1117
Chamberlain, J. W., & Aller, L. H. 1951, ApJ, 114, 52
Christlieb, N., Bessell, M. S., Beers, T. C., et al. 2002, Natur, 419, 904
Christlieb, N., Gustafsson, B., Korn, A. J., et al. 2004, ApJ, 603, 708
Christlieb, N., Schörck, T., Frebel, A., et al. 2008, A&A, 484, 721
Cohen, J. G., Christlieb, N., McWilliam, A., et al. 2004, ApJ, 612, 1107
Cohen, J. G., Christlieb, N., McWilliam, A., et al. 2008, ApJ, 672, 320
Frebel, A. 2010, AN, 331, 474
Frebel, A., Aoki, W., Christlieb, N., et al. 2005, Natur, 434, 871
Frebel, A., Christlieb, N., Norris, J. E., et al. 2006, ApJ, 652, 1585
Frebel, A., Christlieb, N., Norris, J. E., et al. 2007a, ApJ, 660, L117
Frebel, A., & Norris, J. E. 2011, arXiv:1102.1748
Frebel, A., Norris, J. E., Aoki, W., et al. 2007b, ApJ, 658, 534
Frisch, P. C., Redfield, S., & Slavin, J. D. 2011, ARA&A, 49, 237
Fuhrmann, K., Axer, M., & Gehren, T. 1993, A&A, 271, 451
Gallagher, A. 1967, PhRv, 157, 24
García Pérez, A. E., Christlieb, N., Ryan, S. G., et al. 2008, PhST, 133, 014036
Gray, D. F. 1992, The Observation and Analysis of Stellar Photospheres (Cambridge: Cambridge Univ. Press)
Grevesse, N., Asplund, M., & Sauval, A. J. 2007, SSRv, 130, 105
Gustafsson, B., Edvardsson, B., Eriksson, K., et al. 2008, A&A, 486, 951
Heap, S. R., & Lindler, D. 2007, in IAU Symp. 241, Stellar Polpulations as Building Blocks of Galaxies, ed. A. Vazdekis & R. F. Peletier (Cambridge: Cambridge Univ. Press), 95
Heiter, U., Kupka, F., van't Veer-Menneret, C., et al. 2002, A&A, 392, 619
Honda, S., Aoki, W., Ando, H., et al. 2004, ApJS, 152, 113
Keller, S. C., Schmidt, B. P., Bessell, M. S., et al. 2007, PASA, 24, 1
Kupka, F., Piskunov, N., Ryabchikova, T. A., Stempels, H. C., & Weiss, W. W. 1999, A&AS, 138, 119
Lai, D. K., Bolte, M., Johnson, J. A., et al. 2008, ApJ, 681, 1524
Li, H. N., Christlieb, N., Schörck, T., et al. 2010, A&A, 521, A10
Ludwig, H.-G., Behara, N. T., Steffen, M., & Bonifacio, P. 2009, A&A, 502, L1
Luyten, W. J. 1979, NLTT Catalogue: Volume I. +90 to +30, Volume II. +30 to 0 (Minneapolis: Univ. Minnesota)
Luyten, W. J. 1980, NLTT Catalogue: Volume III. 0 to −30 (Minneapolis: Univ. Minnesota)
Mathis, J. S. 1990, ARA&A, 28, 37
McWilliam, A., Preston, G. W., Sneden, C., & Searle, L. 1995, AJ, 109, 2757
Munari, U., Sordo, R., Castelli, F., & Zwitter, T. 2005, A&A, 442, 1127
Norris, J., Bessell, M. S., & Pickles, A. J. 1985, ApJS, 58, 463
Norris, J. E., Christlieb, N., Korn, A. J., et al. 2007, ApJ, 670, 774
Norris, J. E., Gilmore, G., Wyse, R. F. G., Yong, D., & Frebel, A. 2010a, ApJ, 722, L104
Norris, J. E., Ryan, S. G., & Beers, T. C. 1999, ApJS, 123, 639
Norris, J. E., Ryan, S. G., & Beers, T. C. 2001, ApJ, 561, 1034
Norris, J. E., Yong, D., Bessell, M. S., et al. 2013, ApJ, 762, 28 (Paper IV)
Norris, J. E., Yong, D., Gilmore, G., & Wyse, R. F. G. 2010b, ApJ, 711, 350
Oke, J. B. 1965, ARA&A, 3, 23
Pinnington, E. H., Berends, R. W., & Lumsden, M. 1995, JPhB, 28, 2095
Pych, W. 2004, PASP, 116, 148
Ryan, S. G., & Norris, J. E. 1991, AJ, 101, 1835
Ryan, S. G., Norris, J. E., & Beers, T. C. 1996, ApJ, 471, 254
Ryan, S. G., Norris, J. E., & Beers, T. C. 1999, ApJ, 523, 654
Ryan, S. G., Norris, J. E., & Bessell, M. S. 1991, AJ, 102, 303
Schlegel, D. J., Finkbeiner, D. P., & Davis, M. 1998, ApJ, 500, 525
Schörck, T., Christlieb, N., Cohen, J. G., et al. 2009, A&A, 507, 817
Stehlé, C., & Hutcheon, R. 1999, A&AS, 140, 93
Tanner, J., Ryan, S. G., & Norris, J. E. 2006, in Int. Symp. on Nuclear Astrophysics—Nuclei in the Cosmos, ed. A. Mengoni et al. (Trieste: SISSA), PoS(NIC-IX)209
Yong, D., Grundahl, F., Lambert, D. L., Nissen, P. E., & Shetrone, M. D. 2003, A&A, 402, 985
Yong, D., Lambert, D. L., Paulson, D. B., & Carney, B. W. 2008, ApJ, 673, 854
Yong, D., Norris, J. E., Bessell, M. S., et al. 2013a, ApJ, 762, 26 (Paper II)
Yong, D., Norris, J. E., Bessell, M. S., et al. 2013b, ApJ, 762, 27 (Paper III)
York, D. G., Adelman, J., Anderson, J. E., Jr., et al. 2000, AJ, 120, 1579